OXFORD

Human Molecular Genetics, 2015, Vol. 24, No. 22 6473–6484

doi: 10.1093/hmg/ddv356
Advance Access Publication Date: 15 September 2015
Original Article

ORIGINAL ARTICLE

A novel porcine model of ataxia telangiectasia reproduces neurological features and motor deficits of human disease

Rosanna Beraldi[1], Chun-Hung Chan[1], Christopher S. Rogers[2], Attila D. Kovács[1], David K. Meyerholz[3], Constantin Trantzas[4], Allyn M. Lambertz[3], Benjamin W. Darbro[5], Krystal L. Weber[1], Katherine A.M. White[1], Richard V. Rheeden[5], Michael C. Kruer[1], Brian A. Dacken[2], Xiao-Jun Wang[2], Bryan T. Davis[2], Judy A. Rohret[2], Jason T. Struzynski[2], Frank A. Rohret[2], Jill M. Weimer[1,6,†] and David A. Pearce[1,6,†,*]

[1]Children's Health Research Center, Sanford Research, 2301 E. 60 Street North, Sioux Falls, SD 57104, USA, [2]Exemplar Genetics, Sioux Center, IA 51250, USA, [3]Department of Pathology, University of Iowa, Iowa City, IA 52242, USA, [4]ProtoKinetics, LLC, Peekskill, NY 10566, USA, [5]Department of Cytogenetics/Pediatrics, University of Iowa Carver College of Medicine, Iowa City, IA 52241, USA and [6]School of Medicine, University of South Dakota, Sioux Falls, SD 57105, USA

*To whom correspondence should be addressed. Tel: +1 (605)312 6004; Fax: +1 (605)328 0401; Email: david.pearce@sanfordhealth.org

Abstract

Ataxia telangiectasia (AT) is a progressive multisystem disorder caused by mutations in the AT-mutated (*ATM*) gene. AT is a neurodegenerative disease primarily characterized by cerebellar degeneration in children leading to motor impairment. The disease progresses with other clinical manifestations including oculocutaneous telangiectasia, immune disorders, increased susceptibly to cancer and respiratory infections. Although genetic investigations and physiological models have established the linkage of ATM with AT onset, the mechanisms linking ATM to neurodegeneration remain undetermined, hindering therapeutic development. Several murine models of AT have been successfully generated showing some of the clinical manifestations of the disease, however they do not fully recapitulate the hallmark neurological phenotype, thus highlighting the need for a more suitable animal model. We engineered a novel porcine model of AT to better phenocopy the disease and bridge the gap between human and current animal models. The initial characterization of AT pigs revealed early cerebellar lesions including loss of Purkinje cells (PCs) and altered cytoarchitecture suggesting a developmental etiology for AT and could advocate for early therapies for AT patients. In addition, similar to patients, AT pigs show growth retardation and develop motor deficit phenotypes. By using the porcine system to model human AT, we established the first animal model showing PC loss and motor features of the human disease. The novel AT pig provides new opportunities to unmask functions and roles of ATM in AT disease and in physiological conditions.

[†]These authors contributed equally.

Received: May 1, 2015. **Revised:** August 24, 2015. **Accepted:** September 1, 2015

Introduction

Ataxia telangiectasia (AT) is an inherited, progressive, debilitating and multisystem disorder with an incidence of one in 40 000–100 000 live births (1). In addition to the initial clinical manifestations of ataxia, AT patients are prone to develop immune disorders, cancer, respiratory infections and premature death by the second or third decade of life (2–7). Although palliative and pharmacological treatments have modestly improved patient care, limited understanding of underlying mechanisms of AT have hindered therapeutic development. Mutations in the AT-mutated (*ATM*) gene (8,9), which encodes a 370 kDa Ser/Thr kinase, are associated with clinical AT, and more than 80% of AT patients present no functional ATM protein (10,11). ATM is an ubiquitously expressed protein involved with many cell-cycle checkpoints and functions as a DNA damage response protein (12,13) however, the underlying mechanism(s) linking ATM to neurodegeneration remain unclear. Postmortem brain specimens from AT patients have shown neurodegenerative features particularly localized in the cerebellum with extensive Purkinje cell (PC) and granule cell loss (14–16), but the events leading to this neurodegeneration and why *ATM* affects the cerebellum are unknown.

Several *in vitro* and *in vivo* models have been developed to identify either the cell-autonomous nature or the pathophysiological aspects of the disease (17–20). The current murine models carrying mutated *ATM* have shown high fidelity in mimicking the ancillary symptoms of AT disease including tumor predisposition, immunological disorders, lung disease and infertility (19,21–24). However, the hallmark neuropathological phenotypes of PC loss have not been fully recreated to date. Thus, the development of a more phenotypically accurate AT animal model that bridges the gap between human and current animal models and reproduces the neurodegenerative and neurological features of the human disease is needed. Herein, we report the generation and initial characterization of a novel AT porcine model that displays PC loss from birth. Further, the AT pig also develops clinical motor manifestations similar to those seen in humans. The measurable PC loss and motor deficits can be used as metrics to evaluate disease progression and provide quantifiable endpoints for preclinical therapeutics in translational medicine.

Results

Engineering of AT pigs

We developed a novel AT porcine model via homologous recombination and somatic cell nuclear transfer (SCNT). A targeting vector was engineered to disrupt exon 57 of the endogenous *ATM*, which encodes a significant portion of the ATP-binding region within its kinase domain (KD). The targeting vector included a neomycin-resistant cassette (Neo^R) cDNA, and a premature termination stop codon was added upstream of the Neo^R cassette to enhance disruption of the ATM protein mimicking what has been shown in several AT patients (25–28) (Fig. 1A). The targeting vector was packaged in recombinant adeno-associated virus (rAAV2/1), which was then transduced into fetal fibroblasts derived from Yucatan miniature pigs (PFF; Fig. 1B). A similar approach has been used to target porcine *CFTR*, *LDLR*, *TP53* and *SCN5A* (29–32). Following antibiotic selection and PCR screening, $ATM^{+/-}$clones were used for SCNT to generate $ATM^{+/-}$ piglets. Southern blotting confirmed genotypes of these piglets (Fig. 1C).

$ATM^{+/-}$ female and male pigs were mated to establish $ATM^{-/-}$ containing litters, which displayed expected Mendelian inheritance ratios. PCR (data not shown) and Southern blotting confirmed the deletion within exon 57 and the absence of random integration (Fig. 1E). To confirm these animals were deficient for the ATM KD, we performed Western blotting using a specific antibody on the KD in various tissues and fibroblast lines established from the ear of $ATM^{-/-}$ pigs. The ATM KD was absent in all $ATM^{-/-}$-derived tissue and fibroblasts (Fig. 2A and B). Furthermore, as expected, the truncated protein was not detectable (Supplementary Material, Fig. S1).

ATM kinase assay and cytogenetic analysis

A primary function of ATM is to phosphorylate a network of target proteins evoked by genotoxic agents and ionizing radiation (33). To analyze ATM kinase activity, porcine fibroblasts were exposed to 6 Grays (Gy) of ionizing radiation. As expected, phosphorylation of nine ATM targets was increased after ionizing radiation in control fibroblasts compared with unexposed cells (Fig. 2C). However, no change in phosphorylation was observed in $ATM^{-/-}$-derived cells, confirming a lack of kinase activity (Fig. 2C). Moreover, as expected phosphorylation of p53 and Chk2 was increased in control fibroblasts, but only a slight change was detected in mutant fibroblasts.

To detect chromosomal instability in porcine fibroblasts, as seen in cells from AT patients (34–36), cytogenetic analysis was conducted. An increased number of chromosomal breaks were found in fibroblasts derived from $ATM^{-/-}$ pigs when compared with control cells (Fig. 2D).

Cytoarchitecture of the AT cerebellum

To assess for neurodegeneration in AT pigs, we analyzed the cytoarchitecture of the cerebellum at birth (1-d-old) and in adults (4 months and 1 year). PC loss is a hallmark of AT (16,37,38) but has not been demonstrated in any one of the murine models of the disease. At birth, $ATM^{-/-}$ pigs had reduced PC numbers compared with controls and this change persisted in adult $ATM^{-/-}$ pigs (Fig. 3A). Furthermore, we measured the maximal length between PCs (inter-PC distance) to more sensitively evaluate for focal or heterogeneous PC loss and found it to be significantly increased in $ATM^{-/-}$ pigs compared with controls (Fig. 3B). Importantly, both WT and AT pigs showed trends for increased inter-PC distance during postnatal development (Fig. 3A and B). This observation is consistent with increased inter-PC distance seen in infants during the months following birth (39) and further validates this morphometric approach. Defects in PC cytoarchitecture has also been reported to be altered in AT patients (14,40,41), and we found that PCs from $ATM^{-/-}$ pigs had abnormal angles between the soma and primary dendrite in adult stages ($P = 0.019$) (Fig. 3C). The size of PC soma was unchanged (Fig. 3D) arguing against widespread atrophy of the remaining cells. Given that a substantial portion of cerebellar development continues postnatally, with proliferation and migration of cerebellar granule cells, and because this cell population is affected in AT patients (14,37,41), we evaluated the structure of the external (EGL) and internal granule cell layers (IGL) in $ATM^{-/-}$ pigs. No changes were detected in 1-day-old or in adult pigs (Supplementary Material, Table S1). An exception to this was seen in one 4-month-old pig with severe localized cerebellar degeneration/atrophy partially involving two adjacent folia located at the rostral extent of the lateral hemisphere (Fig. 4 and Supplementary Material, Table S2). A similar slight, yet significant, reduction in the thickness of the somatosensory/motor cortex was observed in $ATM^{-/-}$ pigs (Supplementary Material, Fig. S2).

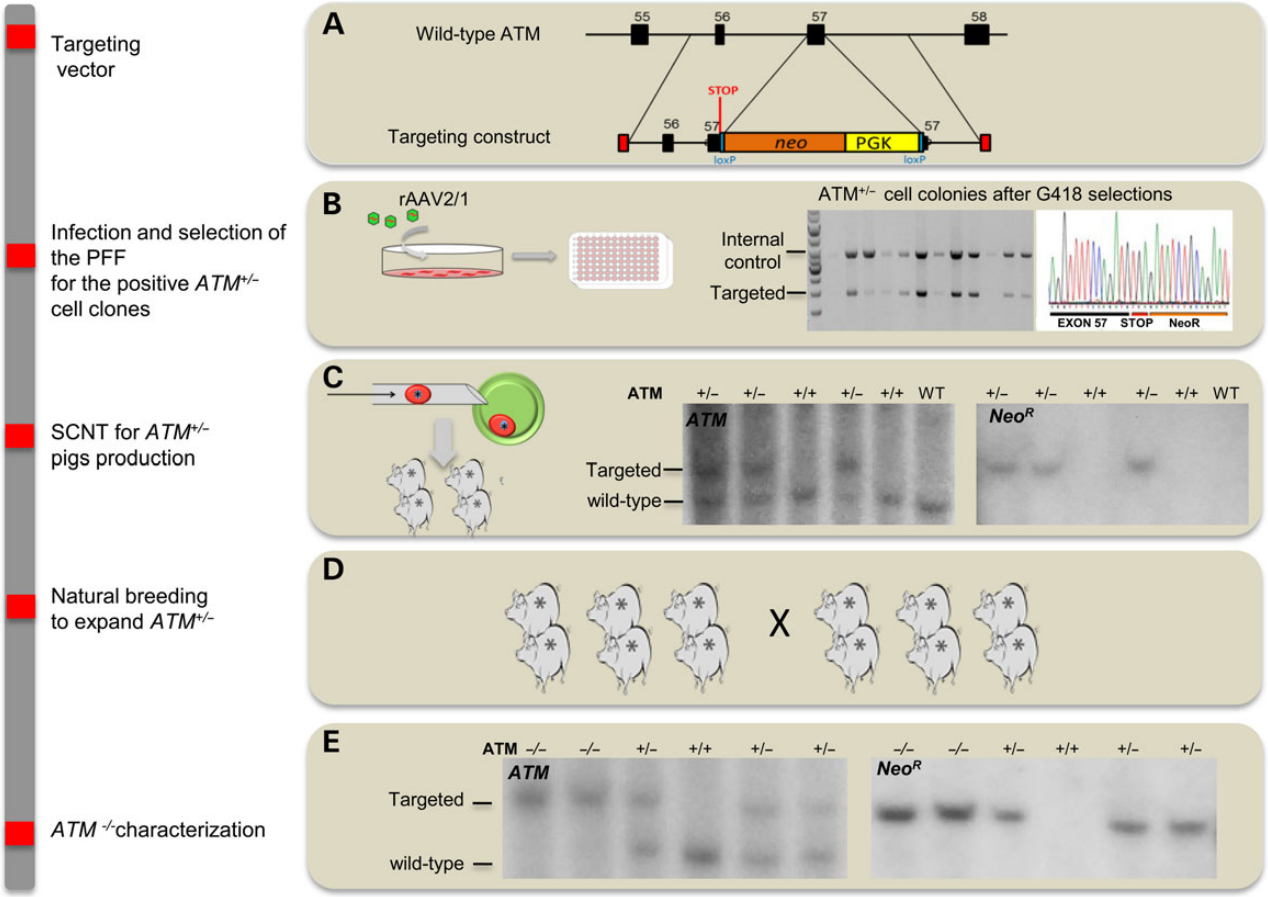

Figure 1. Engineering of ATM-deficient pigs. **A**, the wild-type locus and targeting vector used to disrupt exon 57 of *ATM*. (**B**) Representative PCR screen of seven cell clones upon G418 selection after PFF were infected with recombinant adeno-associated virus (rAAV2/1) containing the targeting vector. The top band (3.8 kb) in each lane represents amplification of endogenous control gene SCN5A while the bottom band (2.0 kb) shows the targeted *ATM* allele. (**C**) Representative genomic Southern blot of $ATM^{+/-}$pigs generated by somatic cells nuclear transfer (SCNT). (**D**) herd expansion of $ATM^{+/-}$pigs to generate the $ATM^{-/-}$ cohort. (**E**) Southern blotting of *Xmn*I digested genomic DNA hybridized to a probe that detects porcine *ATM* downstream of the targeting vector boundary (left blot). The *ATM*- targeted allele produced an ~7.2 kb band, while the wild-type band is ~5.5 kb. The same DNA was hybridized to a probe that detects the Neo^R cassette, yielding only the targeted 7.2 kb band in *ATM*-targeted piglets (right blot).

Clinical phenotype of the AT pigs

We monitored the pig weights throughout the clinical phenotype study, and we found that $ATM^{-/-}$ pigs had reduced weights starting at ~3 months of age that persisted through adulthood (Fig. 5A), recapitulating the growth retardation seen in human patients (42).

To evaluate gait and motor coordination, a customized balance beam was constructed. While control pigs had no problem walking back and forth on the balance beam during 5 min trial intervals (Fig. 5B and Supplementary Material, Video S1), $ATM^{-/-}$ pigs were hesitant to come out of the gate and approach the beam (Supplementary Material, Video S2). Once on the beam, $ATM^{-/-}$ pigs showed instability to stand on the beam, they walked very slowly and they were often incapable of traveling the entire track, trying to turn back after only a few steps (Fig. 5B and Supplementary Material, Video S3).

To further pinpoint specific gait parameters that were perturbed in $ATM^{-/-}$ pigs, we customized a Zeno Electronic Walkway and PKMAS software for use with the porcine model (43). After data collection and processing, we calculated the mean, coefficient of variation (% CV) and fore-to-hind (F/H) hoof symmetry ratio of the following gait measurements: stride time, step time, stance [measured by % gait cycle (GC)], swing (%GC), stride length, step length and integrated pressure (see definitions in Fig Materials and Methods section and in Supplementary Material, Video S4). These gait components are commonly used in the evaluation of humans for detection of neurological and motor conditions including AT. For instance the %CV was calculated because patients with cerebellar ataxia are usually inconsistent and lose their ability to stabilize their walk pattern (44–48).

Interestingly, we identified gait parameter outliers that highlighted the $ATM^{-/-}$ pigs. Specifically, the integrated pressure, stride length, stride time, stance (%GC) and swing (%GC) had increased variations (%CV) in the $ATM^{-/-}$ pigs, recapitulating the variability in gait parameters seen in ataxic patients (44,47–49) (Fig. 5C and D). F/H symmetry ratio of the step time, stance (% GC) and swing (%GC) were also increased in AT pigs compared with the control group.

Discussion

Mouse models of AT have been useful in dissecting various intricate pathophysiological aspects of this disease. Propensity for

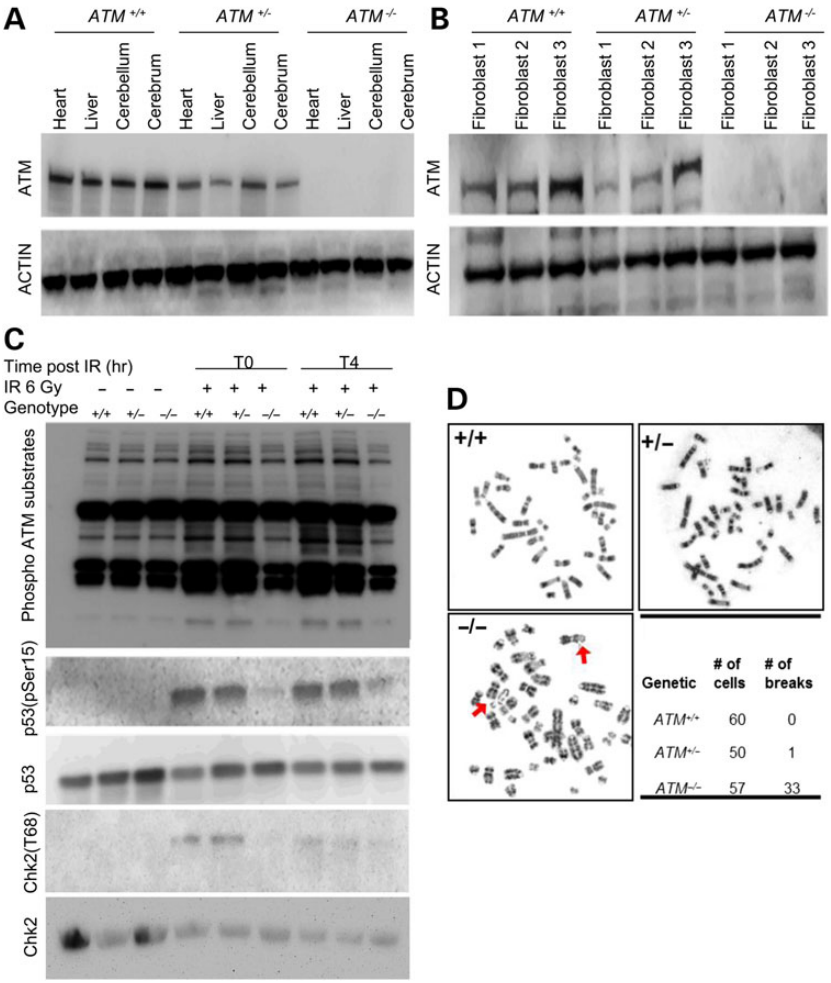

Figure 2. Lack of ATM kinase activity and genomic instability in $ATM^{-/-}$ fibroblasts. (**A**) Western blots from heart, liver, cerebellum and cerebrum tissues harvested from $ATM^{+/+}$, $ATM^{+/-}$and $ATM^{-/-}$ pigs. A slightly reduction of the ATM KD band (~370 kDa) was seen in $ATM^{+/-}$pigs; the band was completely absent in tissue derived from pigs $ATM^{-/-}$ (**B**) Western blotting on three independent fibroblast lines established from $ATM^{+/+}$, $ATM^{+/-}$ and $ATM^{-/-}$ skin biopsies showed similar reduced levels of KD. (**C**) ATM kinase activity in fibroblast lines exposed to ionizing irradiation at 6 Gy. Increased phosphorylation of ATM substrates (top blot) and p53 (Ser15) and Chk2 (Thr68) (middle blot) were seen after 0 and 4 h (T0 and T4) of 6 Gy exposition in $ATM^{+/+}$, $ATM^{+/-}$ fibroblasts while no increased signal was detected in $ATM^{-/-}$ fibroblasts. (**D**) Cytogenetic analysis of chromosomal breaks in fibroblasts showed an increase in chromosomal breakage (arrowheads) in cells derived from $ATM^{-/-}$ pigs.

immune disorders and cancers has been successfully reproduced in rodent models of AT (19,21,22); however, the hallmark neuropathological phenotype has yet to be fully modeled.

Although studies with current mouse models have revealed some novel cellular aspects (50,51) in the cerebellum that may precede the PCs loss seen in human AT patients, AT mice do not display PC degeneration possibly due to cancer development limiting their lifespans (21).

We engineered a novel large animal model of AT to better bridge the gap between patients and the mouse models. Another ATM-targeted pig has recently been reported using similar strategy , however that model is still in early stages, and only the generation of heterozygote females was described without any neurological or behavioral characterization (66). The initial characterizations have shown several neuropathologic and motor features of AT patients (15,16,52,53) suggesting the suitability of the new model to study AT.

Our porcine AT model shows cerebellar lesions with quantifiable PC loss and altered cytoarchitecture at birth. These changes showed nominal progression in the ensuing months after birth, which suggests that AT pathogenesis is prone to appear at various stages of development (e.g. fetal growth and possibly several years after birth). While PC architecture and numbers are not definable in newborn AT infants, the onset of clinical disease several years after birth could support this developmental 'stage' concept in terms of pathogenesis. Overall, our findings suggest the possibility that AT pathogenesis starts with early neurodevelopmental defects and has a neurodegenerative component that could take place a later stage of the disease. The insignificant neurodegenerative changes in our pig model between birth and 1 year can reflect that 1 year is a relatively early stage compared with the normal lifespan of the pig. The premise of ATM's role in fetal development is not new, but consistent with previous studies in humans and mice that have reported the requirement of ATM both in cerebellum and cerebrum development (14,54,55). We showed that PC density in both WT and AT pigs decreased postnatally and this is consistent with PC biology during postnatal development in humans. The reduced PC number in the cerebellum of AT pigs is interesting, as similar studies cannot be performed in humans. In newborns, retrospective autopsy studies or prospective imaging studies are limited by ethical standards, sufficient patient numbers, adequate controls and

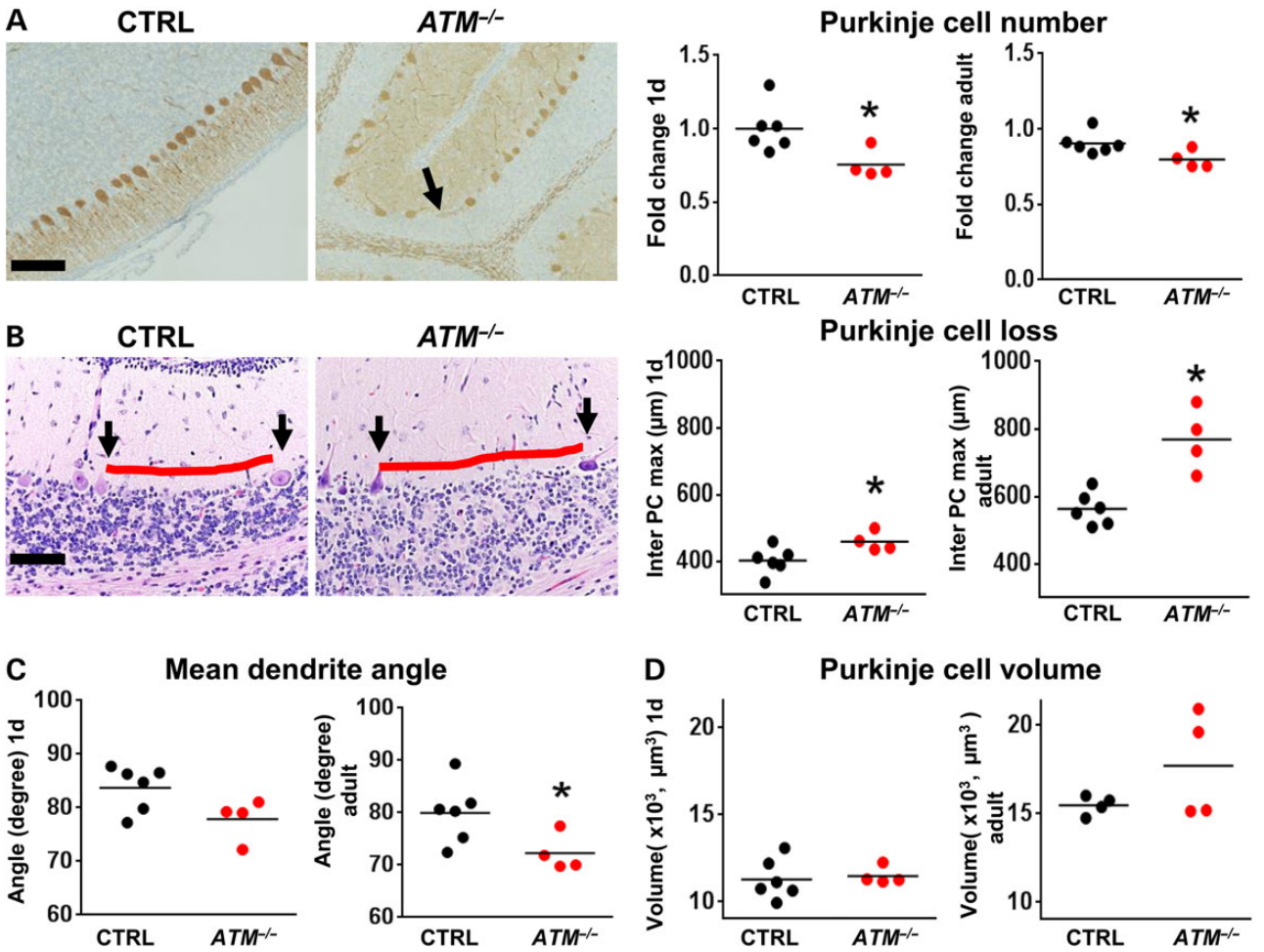

Figure 3. Neurodegeneration in the cerebellum of $ATM^{-/-}$ pigs. (**A**) Compared with controls (CTRL N = six), the cerebellum of $ATM^{-/-}$ pigs (N = five) immunostained with anti-calbindin antibodies (bar 100 µm) had a reduced number of PC (black arrow) on 1 day (left graph, P = 0.02, Mann–Whitney test), and this change remained in adult pigs (right graph, P = 0.02, Mann–Whitney test). (**B**) PC loss (represented by red line length) was also evaluated by maximal inter-PC distance (left and right panels, H&E stain, bar = 100 µm). The inter-PC distance was elevated by ~14% in $ATM^{-/-}$ pigs compared with CTRL at 1d (left graph, P = 0.02, Mann–Whitney test), consistent with reduced PCs (black arrows). This difference increased during postnatal development to ~36% in adults (right graph, P = 0.005, Mann–Whitney test). (**C**) The angle between the soma and the main dendrite of PCs was reduced in A–T pigs at 1 day (left graph, P = 0.057, Mann–Whitney test) and in adults (right graph, P = 0.02, Mann–Whitney test). (**D**) PC volume showed no significant differences between groups at day 1 (left graph) or in adults (right graph, n.s., Mann–Whitney test).

the low sensitivity of imaging techniques required for early lesion assessment (56).

In one 4-month-old AT pig, we observed regional loss/degeneration of PCs, IGCs and cerebellar atrophy features consistent with AT disease (40). This pattern of localized early disease has been reported in imaging studies of young humans in which the disease has preferential origin at localized sites (e.g. superior vermis or lateral cerebellum) (57). Interestingly, some of the remnant PCs in the lesion had evidence of dystrophic calcification a degenerative cellular change that can be preferentially seen in association with several types of brain cell injury (e.g. hypoxia) and in some selected disease (58,59). While brain mineralization is not recognized as a classic AT lesion, it has been reported at autopsy in an AT patient (60). Importantly, there were no histopathological lesions of co-morbidities (e.g. infarction, hemorrhage or infection) which could alternatively explain the regional distribution and mineralization lesions in the cerebellum of this pig. Therefore, we speculate that these manifestations of mineralization in the lesion could represent: (1) early pathologic manifestation(s) of AT disease that are not readily observed from human autopsy cases (that often come from patients with advanced AT disease), (2) altered kinetics of disease between humans and pigs or (3) porcine-model specific manifestation of early cerebellar AT disease. Examination of additional animals at various stages of disease should further define and clarify the pathogenesis of these AT cerebellar lesions.

In AT patients, ataxia is the most common movement disorder encountered, although other movement conditions including dystonia, myoclonus and oculomotor apraxia (52,61–64) have also been described. To evaluate our AT pig model for motor disorder, we developed several behavioral assays to analyze both general and specific gait components customized for large animals. AT pigs had growth retardation starting at 3 months of age, and we simultaneously identified a network of spatio-temporal gait component outliers that were unique to the AT pigs. These findings demonstrate a motor phenotype consistent with our histopathologic findings that may be a valuable metrics of disease progression. However, the chronological onset of gait abnormalities relative to the pathologic defect remains to be defined.

Due to the multifaceted nature of AT, the porcine model can provide a powerful tool to study AT associated cancers, immunologic disorders and lung disease as well as provides a

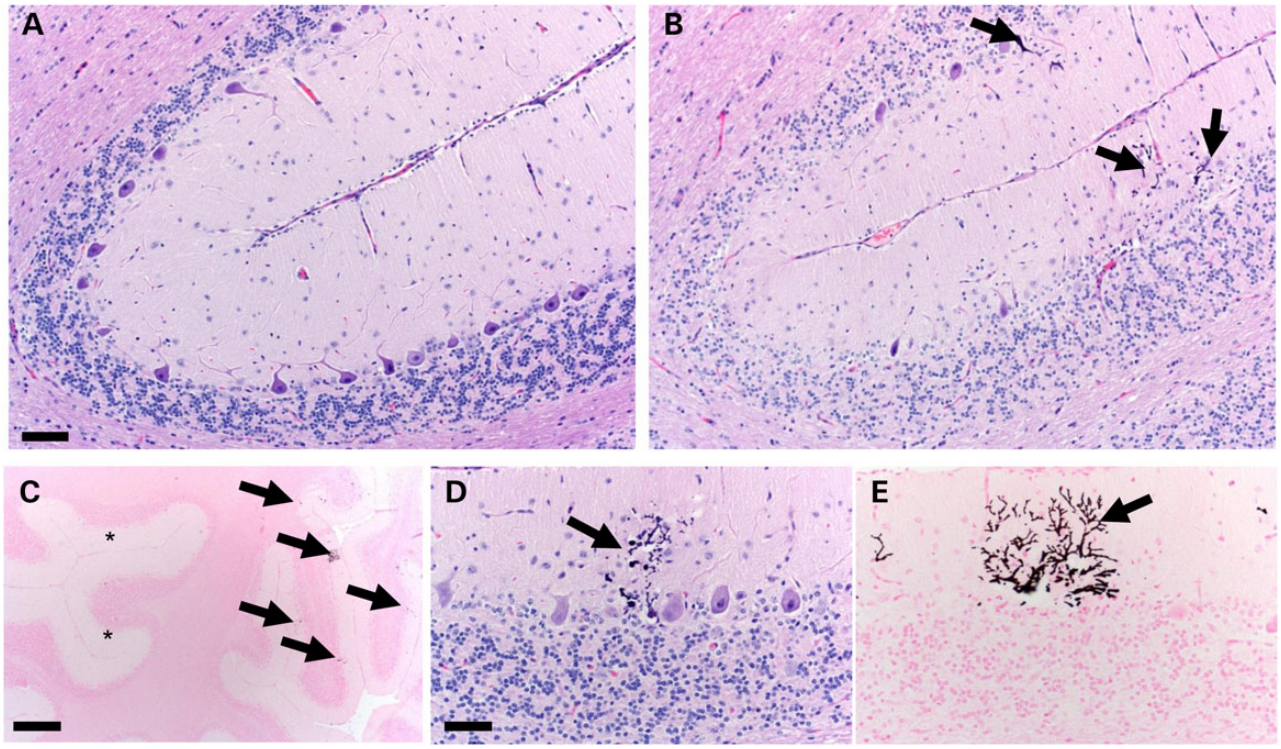

Figure 4. Histopathology of the cerebellum in 4-month-old $ATM^{-/-}$ pig. (**A**) Most of the cerebellum had relatively normal microscopic organization but (**B**) one locally extensive region in the cerebellum had degeneration across multiple adjacent folia characterized by severe thinning of the ML and internal granular layer with loss of PCs (arrows, b, bar 115 µm). (**C**) The interface of intact and degenerate cerebellum shows relatively intact folia (asterisks) and regions containing dystrophic calcification (arrows) with adjacent thinning of folia (Von Kossa stain, bar = 785 µm). (**D** and **E**) Dystrophic mineralization (arrows) was seen in subset of scattered composed of degenerate PCs and their dendritic trees (H&E and Von Kossa stains, respectively, bar 85 µm).

system to refine early diagnostic imaging tools including computed tomography and magnetic resonanace imaging for human AT pathologies. The presence of lymphoma and changes in the concentration of serum alpha fetoprotein (AFP) were not detected in our AT pigs; however, only 3-month- and 1-year-old pigs were examined. For this initial study, we were primarily focused on the establishment of an AT porcine model and the initial evaluation of neuropathology and motor phenotypes. The appearance of lymphoma, changes of serum AFP and other clinical manifestations could be dependent on the age of the pigs and thus merits further investigations.

At this early stage of characterization, the AT pig is the first animal model that mimics some of the neuropathological and motor phenotypes of the human AT. Despite the larger size and higher costs of the porcine compared with the rodent models, its ability to mimic the neuropathological and motor features of AT makes it an attractive model to study AT onset, and to develop new effective treatments. Based on our results, early diagnosis and intervention may be crucial to improve symptoms and/or delay, halt or even reverse later manifestations of the disease.

Our tools for measuring PC loss and the motor deficit components may be useful for further evaluation of the AT porcine model and later for the assessment of novel *in vivo* diagnostic, prognostic and therapeutic protocols for human AT.

Materials and Methods

Yucatan pigs welfare

This study was carried out in accordance with the recommendations of the NRC *Guide for the Care and Use of Laboratory Animals*. All animals were generated and housed in the AAALAC-accredited facilities of Exemplar Genetics. Standard procedures for animal husbandry were used throughout. The Institutional Animal Care and Use Committee of Exemplar Genetics approved all animal experiments. Pigs were housed together in groups with littermates.

Gene-targeting construct

A 10 kb PCR product that included exon 54 to intron 57–58 of *ATM* was amplified from Yucatan miniature pig genomic DNA using high-fidelity polymerase (Platinum *Taq* High Fidelity; Invitrogen) and the primers ATM PCR 2F and ATM PCR 1R (Supplementary Material, Table S4). The PCR product was subcloned into pCR2.1-TOPO (Invitrogen) and sequenced (Supplementary Material, Table S4). This plasmid (referred to as pATM) served as the template for PCR amplification of the 5′ and 3′ homologous targeting arms. The 5′ and 3′ arms of the gene-targeting construct were amplified by PCR using pATM and subcloned into a plasmid containing a PGK-Neo^R cassette. The primers used to amplify the 5′ arm were ATM 5′ arm F (*Xho*I) and ATM 5′ arm R (*Eco*RV) (Supplementary Material, Table S4) and produced the 1,656 bp 5′ homologous arm. The primers for the 3′ arm were ATM 3′arm F (HindIII) and ATM 3′arm R (HindIII) (Supplementary Material, Table S4) which amplified the 1777 bp 3′ homologous arm. This targeting construct (pATM-Neo) was used as a template to create the amplicon for generation of the *ATM*-targeting rAAV proviral vector. PCR amplification of a 4.5 kb amplicon from plasmid pATM-Neo was achieved by using the following primers: AAV-ATM-F (*Not*I) and AAV-ATM-R (*Not*I) (Supplementary Material, Table S4). This product was subcloned into the rAAV proviral vector, pFBAAV2-CMVP.NpA and grown in Sure2 cells (Stratagene) to

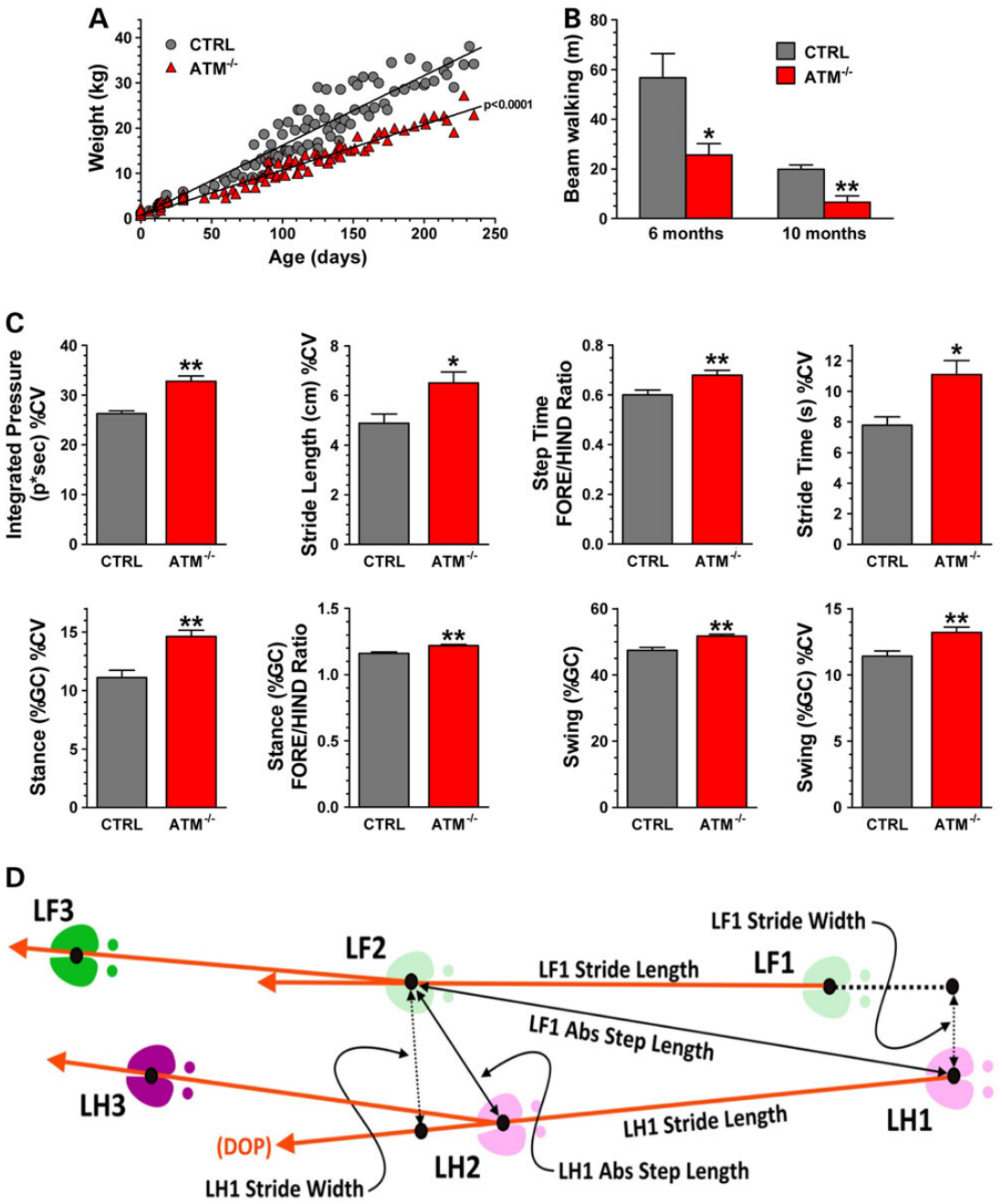

Figure 5. Impaired growth and ataxia manifestation in $ATM^{-/-}$ pigs. (**A**) Pig weight was collected weekly over 250 days from controls (CTRLs $N = six$) and $ATM^{-/-}$ pigs ($N = six$) female pigs. Each symbol (circle CTRL; triangle for $ATM^{-/-}$) represents an individual weight measurement. Growth rates analyzed by linear regression and slopes of the fitted lines were analyzed by unpaired *t*-test ($P < 0.0001$). The weight difference between CTRL and AT pigs became statistically significant at the 97-day-old ($P < 0.01$, two-way ANOVA with Bonferroni's post-test for pairwise multiple comparisons). (**B**) The walking distance over a period of 5 min of age- and gender-matched pigs ($N = four$ per group) was measured on the balance beam at indicated ages (unpaired *t*-test; $^{*}P = 0.0273$, $^{**}P = 0.0053$). (**C**) The graphs represent the mean value of the indicated variables calculated from 66 walks of six CTRLs and from 61 walks of five $ATM^{-/-}$ pigs collected during several sessions and ± SD among walks of each group. The difference between the two groups was determined by Wilcoxon non-parametric test ($^{*}P \leq 0.05$ and $^{**}P \leq 0.002$). (**D**) The scheme depicts the relationship of spatial measurements stride length, absolute step length and stride width for the left fore (LF) and left hind (LH) hooves. The dimensions are scaled for clarity. DOP, Direction of Progression.

ensure inverted terminal repeat integrity. This proviral plasmid is referred to as pAAV-ATM-Neo. The rAAV was packaged by the University of Iowa Gene Transfer Vector Core.

Gene targeting, selection and screening

Approximately 1.0×10^6 passage zero Yucatan porcine fetal fibroblasts (PFF) were plated on 100 mm collagen-coated culture dishes containing PFF media [F10 media (Invitrogen), 20% fetal calf serum (Hyclone), and 30 μg/ml gentamicin]. Cells were transduced with rAAV-ATM-Neo (41 μl, 2.03×10^{13} vg/ml) 24 h after plating. Cells were then split 24 h later by trypsin and re-plated on 96-well collagen-coated plates at a density of 200 cells per well. Selection was initiated 48 h later with G418 (100 μg/ml). Ten days later transduced cells were split among three 96-well plates (one plate for freezing, one for propagation and one for

immediate PCR screening). Approximately 50% of wells contained live cell colonies following selection. Cells in the 96-well PCR plate were lysed (50 mM KCl, 1.5 mM MgCl2, 10 mM Tris–Cl, pH [8.5], 0.5% Nonidet P40, 0.5% Tween, 400 µg/ml Proteinase K) and then incubated at 65°C for 30 min, followed by 95°C for 10 min. Lysates were then used for PCR with the following primers and reaction conditions: ScreenF (NeoR), ATM 4PCR R1, SCN5A seq6 F and SCN5A kpnI probe R2 (Supplementary Material, Table S4) 2 min at 94°C, 30 cycles of 94°C for 20 s, 58°C for 10 s and 68°C for 4 min, and finally 68°C for 7 min. The expected product for the targeted allele was 2.0-kb and a 3.8-kb product from the *SCN5A* internal control. PCR-positive cells were grown to 100% confluence and either cryo-preserved or expanded for DNA isolation. High-molecular weight genomic DNA was isolated from pig umbilicus (Qiagen) and digested with *Xmn*I. Southern blot was performed as previously described (29) using *ATM*- and Neo^R-specific probes, which were amplified with the following primers: ATM *Xmn*I probe 1F/ATM *Xmn*I probe 1R and PGK-NeoF/NeoR-R, respectively (Supplementary Material, Table S4). The *ATM*-targeted allele produced an ~7.2 kb band, while the wild-type band is ~5.5 kb. The same DNA was hybridized to a probe that detects the Neo^R cassette, yielding only the targeted 7.2 kb band.

Nuclear transfer

Nuclear transfer was performed by Viagen, Inc. (Austin, TX) as previously described (65). Briefly, *ATM*-targeted PFF were collected in salt-buffered NCSU-23 containing 10% fetal calf serum and transferred into the oocytes. Oocytes were matured in Earle's TC199-HEPES supplemented with 5 mg/ml insulin, 10 ng/ml epidermal growth factor, 0.6 mM cysteine, 0.2 mM sodium pyruvate, 25 mg/ml gentamicin, 5 mg/ml follicle stimulant hormone and 10% porcine follicular fluid for 40 h prior to manipulation.

Embryo transfer

Embryo transfer was performed at Exemplar Genetics. Briefly, reconstructed oocytes were transferred into synchronized post-pubertal domestic gilts on the first day of standing estrus. Recipient gilts were preanesthetized with intravenous propofol (0.5–5 mg/kg) and anesthesia was maintained with inhaled isoflurane (3–5% in oxygen via face mask). Following a midline incision to access the uterus, reconstructed embryos were transferred into the oviduct at the ampullary–isthmus junction. Intra- and post-operative analgesia was provided by intramuscular injection of flunixin meglumine (2.2 mg/kg). Recipient animals were tested for pregnancy by abdominal ultrasound after Day 21 and throughout gestation.

Organ collection and skin fibroblast generation

Heart, liver, cerebellum and cerebrum were harvested from 1-day, 4-month and 1 year-old euthanized pigs ($ATM^{+/+}$$ATM^{+/-}$ and $ATM^{-/-}$). Half of each collected tissue type was placed in either 10% neutral buffered formalin for 8–10 d at room temperature or stored at −80°C for Western blotting.

To establish fibroblast lines for *in vitro* study, 6 mm ear punch biopsies were taken from 1-day-old $ATM^{+/+}$, ATM^{+-} and $ATM^{-/-}$ anesthetized pigs. Each ear punch was immediately placed in high glucose Dulbecco's Modified Eagle's Medium (DMEM, Hyclone) containing 1% of Pen-Strep (Fisher). In a sterile hood, skin biopsies were chopped into smaller pieces and incubated overnight in DMEM digestion media containing 20% fetal bovine serum (Fisher), 100 mg collagenase type I (Worthington-Biochem), 20 mg DNAse-I (Sigma) and 1% Pen-Strep at 37°C in an equilibrated CO_2 chamber and under sterile conditions. Cells were passaged upon confluence in high glucose DMEM supplemented with 10% fetal bovine serum, 1% non-essential amino acids (Invitrogen) and 1% Pen-Strep.

Cell irradiation and ATM kinase assay

Porcine skin fibroblasts were cultured for no more than two passages. Cells were cultured for 2 days and then irradiated with 6 Gy of radiation (RS 2000 Rad × Ray machine, Rad Source Technologies, Inc.). The cells lysates in radioimmunoprecipitation assay (67) were either collected immediately after (T0) or 4 h after radiation exposure (T4). A baseline was represented by cells with no irradiation.

Western blotting

Porcine organs and skin fibroblasts *in vitro* were lysed in ice-cold RIPA buffer and used for immunoblotting as previously described (68). In brief, a total of 30 µg of protein was subjected to NuPAGE 3% gel electrophoresis. Separated proteins were then transferred onto nitrocellulose membranes overnight at 30 V and 4°C. Blots were probed with: anti-ATM KD (Thermo scientific, cat # MA1-23152; 1:1000), anti-ATM recognizing a central region of ATM protein (Abbiotec, cat # 200158; 1:1000), anti-β-actin (Sigma; cat # A5441-100; 1:10 000) as a loading control. For the phosphorylation assay, anti-phospho (Ser/Thr) ATM/ATR (Cell Signaling; cat # 6966 1:1000) was used to probe the phosphorylation status of nine ATM substrates containing S*/T*Q motif. Anti-phospho p53 (pSer15) (Cell Signaling; cat # 9284S 1:1000) and anti-phospho-Chk2 (Thr68) (Cell Signaling cat # 2197, 1:1000) were used to test the phosphorylation status of two specific ATM substrates. P53 antibody (Millipore cat #OP03, 1:1000) and Chk2 (cell signaling cat # 6334, 1:1000) were used to test the total proteins, respectively.

Cytogenetic analysis

$ATM^{+/+}$, $ATM^{+/-}$and $ATM^{-/-}$ pig fibroblast were established and cultured *in vitro* for only two passages before cytogenetic analysis. Those cells with no clastogenic treatment were examined. No ethidium bromide or other intercalating agents were utilized during the chromosome harvest. Metaphase figures were scored for breakage using standard cytogenetic methods (69,70).

Histopathology and morphometric analysis

Cerebella were obtained from $ATM^{+/+}$, $ATM^{+/-}$ and $ATM^{-/-}$ pigs at different ages: 1 day: $ATM^{+/+}$ (two female and two male), $ATM^{+/-}$ (two male) and $ATM^{-/-}$ (two female and two male) ; 4 months: $ATM^{+/+}$ (two female and one male), $ATM^{+/-}$ (one female and one male) and $ATM^{-/-}$ (two female and one male); 1-year $ATM^{+/+}$ (one female) and $ATM^{-/-}$(one female). Due to a lack of overt differences, the 4-month and 1-year samples were combined for analysis as the 'adult' group, while $ATM^{+/+}$ and $ATM^{+/-}$ sample were combined and labeled as control (CTRL). The cerebella were harvested, separated into two hemispheres through the vermis, and preserved in 4% paraformaldehyde for 8–10 d before proceeding with histopathological analysis. Hemispheres were cut perpendicular to the vermis to separate the rostral and caudal portions; the rostral portion was subsequently processed for immunohistochemistry. Forty paraffined 5-µm serial sections were cut, orienting sections from the vermis throughout the flocculus.

For each pig's cerebellum, three equidistant sections were analyzed corresponding to the external (vermis), central and internal (flocculus) regions of the cerebellum. Immunostaining was performed using anti-calbindin antibodies (Cell Signaling cat # 2136, 1:5000) and hematoxylin counterstain to assess PC number, morphology and nuclei. Only PCs within the section showing a clear nucleus were counted. An anti-Ki67 antibody (BioCare Medical cat # CRM325A; 1:100) was used to mark proliferation in the EGL. Histochemical staining included standard hematoxylin and eosin (H&E) (71) staining for routine tissue examination and Von Kossa staining for detection of calcification in PCs (72). Images were collected using a ×20 objective (Nikon P091), and PC numbers and angle degree between the soma and principal dendrite were calculated using Nikon NIS Elements software. The total number of PCs and the angle reported for each sample represents the average of three sections examined. For volumetric quantification of the soma, the nucleator method (73) was used. Briefly, three sequential 50 µm sections for each cerebellum were cut by vibratome and stained with Calbindin antibodies and hematoxylin. Approximately, 100 cells per cerebellum were measured using Microbrightfield Nucleator software (Stereo Investigator version 10). Five rays were used to estimate the volume of the cells, five points of intersection of randomly rotated radii with the nuclear and cell border were marked .The PC soma volume were estimated from the lengths of radial cellular segments using the center of the nucleus as a reference point. The mean coefficient of error for Nucleator estimates was calculated according to the Gunderson and Jensen method (74) and was <0.08.

Tissues were evaluated by an ACVP-boarded pathologist using standard principles of morphometric analysis and histopathologic scoring (75) using a BX53 microscope, high-resolution DP73 digital camera and CellSens software (Olympus, Center Valley, PA, USA). All analyses in this paragraph were done with HE stained tissues unless otherwise stated. Mean tissue thickness for the molecular layer (ML), IGL and EGL was evaluated by defining the total area of each layer and dividing by length of the layer being evaluated for an average thickness as previously described (76). The EGL was also evaluated for retention or altered migration into the ML by measuring the maximum EGL thickness in each tissue section, avoiding areas of sectioning artifact. Additionally, IGL was evaluated in which areas of least cellularity (assay for focal loss) were enumerated for nuclei per ×600 image field. Given the lack in understanding of AT pathogenesis and early PC loss, we assessed PC numbers from three perspectives. (1) PC soma were enumerated (RB) from Calbindin stained sections and divided by the length of ML and IGL interface to give the incidence (cells per length). (2) PC soma were enumerated (DKM) from HE stained sections and divided by the length of tissue along the ML and IGL interface to give the incidence (cells per length). (3) As an alternative approach inter-PC distance, a previously validated approach to measure PC loss (77), was measured (DKM) and the three maximal values for each animal were averaged to generate a mean maximal value/animal. We chose maximal inter-PC distance to morphometrically detect change (i.e. increased inter-PC distance) in tissues because in our experience in morphometry (DKM) this can have higher sensitivity to detect focal change than does averages. Since approaches, #1 and #2 had similar results and since they were evaluated by different observers (which are strength in morphometric analysis)—we merged these results for reporting purposes. Values from each analysis were normalized to 1-day-old CTRL pigs as 'fold change', and these results from each observer were averaged for each pig for a final reporting of data as 'fold change' relative to 1-day-old CTRL.

For cortical thickness measurements, 4 month CTRL (two female) and ATM$^{-/-}$ (two female) old brains were blocked to remove primary motor, somatosensory and premotor cortex. Fifty micrometer sections from each cortices were analyzed. The sections were prepared on a vibratome and incubated in DAPI fluorescent dye for 30 min using a standard protocol. Tiled images were captured using a Nikon NI-E Microscope with NIS-Elements Advanced Research Imaging Software Version 4.30.01 at an objective of ×2. Using the software's length tool, the thickness of the cortical plate (as depicted in Supplementary Material, Fig. S2) was measured in triplicates at three different medial–lateral positions as denoted in the schematic.

Phenotyping

A customized 2.43 m long and 0.17 m wide balance beam was made to assay the balance and gait of four female ATM$^{+/+}$ and wild-type (CTRL) and four female *ATM*$^{-/-}$ pigs. The beam was modifiable in order to accommodate the changing size of pigs throughout the experiment time-course. The outside of the apparatus consisted of a rectangular box measuring 3.65 m long by 0.76 m wide by 0.86 m tall with an open top and bottom. This outer box was intended to contain the pig during trials and included a door on one end to allow the pigs to enter and exit the apparatus. Inside the outer box was a raised deck ~0.20 m off the floor. The raised deck consisted of a 0.6 × 0.76 m platform on each end where the pigs could turn around. Between the two platforms was a beam that measured 2.43 m long (also 0.20 m off the floor) and was adjustable in width up to 0.17 m based on the size of the pigs. All walking surfaces were covered in non-slip adhesive strips to improve traction. A railing was in place on both sides of the beam to prevent the pig from falling to the ground and injuring itself.

The pigs were subjected to training periods of 3 weeks before beginning data collection. The animals were assayed in the morning under fasting conditions and after 1 h of acclimation in the room where the balance beam was located to avoid environmental factors that could interfere with their behavior.

Zeno walkway and PKMAS software for spatio-temporal gait components analysis

To collect gait measurements we utilized a Zeno Electronic Walkway (ZenoMetrics Peekskill, NY) and PKMAS Software (Protokinetocs LLC, Havertown, PA). The advanced features of the Zeno walkway, typically used with human subject, were customized for use with pigs. The Zeno walkway was 4.87 m long by 0.6 m wide and sampled at 120 Hz (43).

The Zeno electronic walkway was enclosed by side panels and a space of 1 m was allocated on both ends to allow the pig to make a turn outside the active area of the electronic walkway. The pigs have been trained and were enticed to walk across the electronic walkway by receiving a treat at the end of each walk. Spatio-temporal parameters were collected from the walks of ATM$^{+/+}$ and wild-type (N = six female ranging in age from 3–15 months) and *ATM*$^{-/-}$ (N = five females ranging in age from 3–15 months) pigs. There was no statistical difference between ages of the two groups. For each pig, we collected data from a minimum of six walking trials during each session. A trial was valid if all four hooves were within the walkway and by visually inspecting if the pig completed the walk without hesitation. Data were processed discarding four hooves at the beginning and end of the walkway.

The Zeno System collected data from the following measurements: stride time, step time, stance time, swing time, stride length, step length and pressure. In addition to the collected data the PKMAS software calculated stride velocity, stance and swing as a percentage of stride time (gait cycle), integrated pressure over the period of stance time and symmetry ratios for the fore/hind limbs. In order to minimize the effects of velocity on gait parameters, we accepted trials with a velocity range 96–160 cm/s. For each trial we exported, the trial mean, the trial coefficient of variation (%CV) and the trial F/H hoof symmetry ratio of the following gait measurements: stride time, step time, stance (%GC), swing (%GC), stride length, step length and integrated pressure. Spatial measurements utilize the center of the ellipse as the point of measurement and followed the definitions of Huxham, F (78).

Step time (s): the time between consecutive first contacts of the opposite hooves (same side).

Step length (cm): the distance between opposite consecutive hooves (same side).

Stride length (cm): the distance between the same consecutive hooves. The vector connecting the center points between these two hooves is the Direction of Progression (DOP).

Swing time (s): the time a hoof is not in contact with the ground.

Stance time (s): the time a hoof is in contact with the ground.

Stride time (s): synonymous to Gait Cycle Time (GC): the time elapsed between first contact of one hoof, to the following first contact of the same hoof.

Stance (*%GC*): stance time expressed as a percentage of stance time/(GC)

Swing (*%GC*): swing time expressed as a percentage of Stride Time/(GC)

Stride velocity (cm/s): the ratio of Stride Length to Stride Time.

Stride width (cm): the length of the perpendicular line connecting the points between two ipsilateral hooves (the stride line) with the center of the contralateral hoof.

%CV: coefficient of variation was calculated using the formula $(\%\mathrm{CV} = (100 \times \mathrm{SD})/\mathrm{mean})$.

Statistical Analysis

Statistical analysis was performed using Prism software (v6.0, Graphpad Software, La Jolla, CA, USA). Comparisons of cerebellar structure of CTRL and AT samples were performed with one-tailed non-parametric Mann–Whitney test. The gait parameters were analyzed utilizing the Wilcoxon non-parametric test; the difference was considered significant when ($P \leq 0.05$). The post hoc Bonferroni correction was applied and considering the 23 gait parameters we analyzed, the difference was accepted as statistically significant when ($P \leq 0.002$). The beam walking performance of CTRL and $ATM^{-/-}$ pigs were compared by two-tailed, unpaired *t*-test. Weight differences were determined by two-way ANOVA with Bonferroni's post-test for pairwise multiple comparisons.

Supplementary Material

Supplementary Material is available at *HMG* online.

Acknowledgements

We thank Dr Alexei Savinov (Sanford Research) for assistance in necropsy and Dr Satoshi Nagata (Sanford Research) for the valuable feedback on immunological aspect of the disease. Assistance was provided by the Sanford Research Molecular Pathology and Imagining Core and by the University of Iowa Carver College of Medicine, Comparative Pathology Laboratory for assistance with histological analysis. We thank Dr Miranda Bader for critical review of the manuscript, and Ryan Geraets and Logan Langin for help with the pig behavior study.

Conflict of Interest statement. C.S.R., X.J.W., B.A.D., B.T.D., J.A.R., J.T.S. and F.A.R. are employees of Exemplar Genetics, a company that has applied for a patent related to the work reported herein.

Funding

This work was supported by Sanford Research and the National Institute of Health COBRE Projects (grant number P20 GM103620, P20 GM103548) 1R01NS082283 to J.M.W. and by a National Institute of Health SBIR grant to Exemplar Genetics (grant number R44NS076075).

References

1. Swift, M., Morrell, D., Cromartie, E., Chamberlin, A.R., Skolnick, M.H. and Bishop, D.T. (1986) The incidence and gene frequency of ataxia-telangiectasia in the United States. *Am. J. Hum. Genet.*, **39**, 573–583.
2. Makis, A., Polychronopoulou, S. and Haidas, S. (2004) Osteosarcoma as a second tumor after treatment for primary non-Hodgkin's lymphoma in a child with ataxia-telangiectasia: presentation of a case and review of possible pathogenetic mechanisms. *J. Pediatr. Hematol. Oncol.*, **26**, 444–446.
3. Bott, L., Lebreton, J., Thumerelle, C., Cuvellier, J., Deschildre, A. and Sardet, A. (2007) Lung disease in ataxia-telangiectasia. *Acta Paediatr.*, **96**, 1021–1024.
4. Suarez, F., Mahlaoui, N., Canioni, D., Andriamanga, C., d'Enghien, C.D., Brousse, N., Jais, J.P., Fischer, A., Hermine, O. and Stoppa-Lyonnet, D. (2014) Incidence, presentation, and prognosis of malignancies in ataxia-telangiectasia: a report from the French National Registry of Primary Immune Deficiencies. *J. Clin. Oncol.*, in press.
5. Taylor, A.M., Metcalfe, J.A., Thick, J. and Mak, Y.F. (1996) Leukemia and lymphoma in ataxia telangiectasia. *Blood*, **87**, 423–438.
6. Harnden, D.G. (1994) After-thoughts and conclusions on the nature of the A-T gene. *Int. J. Radiat. Biol.*, **66**, S199–S201.
7. Syllaba, L. and Henner, K. (1926) Contribution à l'indépendance de l'athétose double idiopathique et congénitale. Atteinte familiale, syndrome dystrophique, signe du reséau vasculaire conjonctival, intégrité psychique. *Rev. Neurol.*, **1**, 541–562.
8. Gatti, R.A., Berkel, I., Boder, E., Braedt, G., Charmley, P., Concannon, P., Ersoy, F., Foroud, T., Jaspers, N.G., Lange, K. *et al.* (1988) Localization of an ataxia-telangiectasia gene to chromosome 11q22–23. *Nature*, **336**, 577–580.
9. Savitsky, K., Bar-Shira, A., Gilad, S., Rotman, G., Ziv, Y., Vanagaite, L., Tagle, D.A., Smith, S., Uziel, T., Sfez, S. *et al.* (1995) A single ataxia telangiectasia gene with a product similar to PI-3 kinase. *Science*, **268**, 1749–1753.
10. Gilad, S., Khosravi, R., Shkedy, D., Uziel, T., Ziv, Y., Savitsky, K., Rotman, G., Smith, S., Chessa, L., Jorgensen, T.J. *et al.* (1996) Predominance of null mutations in ataxia-telangiectasia. *Hum. Mol. Genet.*, **5**, 433–439.
11. Byrd, P.J., McConville, C.M., Cooper, P., Parkhill, J., Stankovic, T., McGuire, G.M., Thick, J.A. and Taylor, A.M. (1996) Mutations revealed by sequencing the 5′ half of the gene for ataxia telangiectasia. *Hum. Mol. Genet.*, **5**, 145–149.

12. Rotman, G. and Shiloh, Y. (1998) ATM: from gene to function. *Hum. Mol. Genet.*, **7**, 1555–1563.
13. Brown, K.D., Barlow, C. and Wynshaw-Boris, A. (1999) Multiple ATM-dependent pathways: an explanation for pleiotropy. *Am. J. Hum. Genet.*, **64**, 46–50.
14. Vinters, H.V., Gatti, R.A. and Rakic, P. (1985) Sequence of cellular events in cerebellar ontogeny relevant to expression of neuronal abnormalities in ataxia-telangiectasia. *Kroc Found. Ser.*, **19**, 233–255.
15. Aguilar, M.J., Kamoshita, S., Landing, B.H., Boder, E. and Sedgwick, R.P. (1968) Pathological observations in ataxia-telangiectasia. A report of five cases. *J. Neuropathol. Exp. Neurol.*, **27**, 659–676.
16. Paula-Barbosa, M.M., Ruela, C., Tavares, M.A., Pontes, C., Saraiva, A. and Cruz, C. (1983) Cerebellar cortex ultrastructure in ataxia-telangiectasia. *Ann. Neurol.*, **13**, 297–302.
17. Rimkus, S.A., Katzenberger, R.J., Trinh, A.T., Dodson, G.E., Tibbetts, R.S. and Wassarman, D.A. (2008) Mutations in String/CDC25 inhibit cell cycle re-entry and neurodegeneration in a *Drosophila* model of Ataxia telangiectasia. *Genes Dev.*, **22**, 1205–1220.
18. Imamura, S. and Kishi, S. (2005) Molecular cloning and functional characterization of zebrafish ATM. *Int. J. Biochem. Cell Biol.*, **37**, 1105–1116.
19. Barlow, C., Hirotsune, S., Paylor, R., Liyanage, M., Eckhaus, M., Collins, F., Shiloh, Y., Crawley, J.N., Ried, T., Tagle, D. *et al.* (1996) Atm-deficient mice: a paradigm of ataxia telangiectasia. *Cell*, **86**, 159–171.
20. Carlessi, L., Fusar Poli, E., Bechi, G., Mantegazza, M., Pascucci, B., Narciso, L., Dogliotti, E., Sala, C., Verpelli, C., Lecis, D. *et al.* (2014) Functional and molecular defects of hiPSC-derived neurons from patients with ATM deficiency. *Cell Death Dis.*, **5**, e1342.
21. Xu, Y., Ashley, T., Brainerd, E.E., Bronson, R.T., Meyn, M.S. and Baltimore, D. (1996) Targeted disruption of ATM leads to growth retardation, chromosomal fragmentation during meiosis, immune defects, and thymic lymphoma. *Genes Dev.*, **10**, 2411–2422.
22. Elson, A., Wang, Y., Daugherty, C.J., Morton, C.C., Zhou, F., Campos-Torres, J. and Leder, P. (1996) Pleiotropic defects in ataxia-telangiectasia protein-deficient mice. *Proc. Natl. Acad. Sci. U.S.A.*, **93**, 13084–13089.
23. Eickmeier, O., Kim, S.Y., Herrmann, E., Doring, C., Duecker, R., Voss, S., Wehner, S., Holscher, C., Pietzner, J., Zielen, S. *et al.* (2014) Altered mucosal immune response after acute lung injury in a murine model of Ataxia Telangiectasia. *BMC Pulm. Med.*, **14**, 93.
24. Gatti, R.A. and Good, R.A. (1971) Occurrence of malignancy in immunodeficiency diseases. A literature review. *Cancer*, **28**, 89–98.
25. Lai, C.H., Chun, H.H., Nahas, S.A., Mitui, M., Gamo, K.M., Du, L. and Gatti, R.A. (2004) Correction of ATM gene function by aminoglycoside-induced read-through of premature termination codons. *Proc. Natl. Acad. Sci. U.S.A.*, **101**, 15676–15681.
26. Du, L., Damoiseaux, R., Nahas, S., Gao, K., Hu, H., Pollard, J.M., Goldstine, J., Jung, M.E., Henning, S.M., Bertoni, C. *et al.* (2009) Nonaminoglycoside compounds induce readthrough of nonsense mutations. *J. Exp. Med.*, **206**, 2285–2297.
27. Gumy-Pause, F., Wacker, P. and Sappino, A.P. (2004) ATM gene and lymphoid malignancies. *Leukemia*, **18**, 238–242.
28. Brown, K.D., Ziv, Y., Sadanandan, S.N., Chessa, L., Collins, F.S., Shiloh, Y. and Tagle, D.A. (1997) The ataxia-telangiectasia gene product, a constitutively expressed nuclear protein that is not up-regulated following genome damage. *Proc. Natl. Acad. Sci. U.S.A.*, **94**, 1840–1845.
29. Sieren, J.C., Meyerholz, D.K., Wang, X.J., Davis, B.T., Newell, J.D. Jr, Hammond, E., Rohret, J.A., Rohret, F.A., Struzynski, J.T., Goeken, J.A. *et al.* (2014) Development and translational imaging of a TP53 porcine tumorigenesis model. *J. Clin. Invest.*, **124**, 4052–4066.
30. Rogers, C.S., Stoltz, D.A., Meyerholz, D.K., Ostedgaard, L.S., Rokhlina, T., Taft, P.J., Rogan, M.P., Pezzulo, A.A., Karp, P.H., Itani, O.A. *et al.* (2008) Disruption of the CFTR gene produces a model of cystic fibrosis in newborn pigs. *Science*, **321**, 1837–1841.
31. Davis, B.T., Wang, X.J., Rohret, J.A., Struzynski, J.T., Merricks, E.P., Bellinger, D.A., Rohret, F.A., Nichols, T.C. and Rogers, C.S. (2014) Targeted disruption of LDLR causes hypercholesterolemia and atherosclerosis in Yucatan miniature pigs. *PLoS ONE*, **9**, e93457.
32. Park, D.S., Cerrone, M., Morley, G., Vasquez, C., Fowler, S., Liu, N., Bernstein, S.A., Liu, F.Y., Zhang, J., Rogers, C.S. *et al.* (2014) Genetically engineered SCN5A mutant pig hearts exhibit conduction defects and arrhythmias. *J. Clin. Invest.*, **125**, 403–412.
33. Canman, C.E., Lim, D.S., Cimprich, K.A., Taya, Y., Tamai, K., Sakaguchi, K., Appella, E., Kastan, M.B. and Siliciano, J.D. (1998) Activation of the ATM kinase by ionizing radiation and phosphorylation of p53. *Science*, **281**, 1677–1679.
34. Meyn, M.S. (1993) High spontaneous intrachromosomal recombination rates in ataxia-telangiectasia. *Science*, **260**, 1327–1330.
35. Pecker, I., Avraham, K.B., Gilbert, D.J., Savitsky, K., Rotman, G., Harnik, R., Fukao, T., Schrock, E., Hirotsune, S., Tagle, D.A. *et al.* (1996) Identification and chromosomal localization of Atm, the mouse homolog of the ataxia-telangiectasia gene. *Genomics*, **35**, 39–45.
36. Meyn, M.S. (1995) Ataxia-telangiectasia and cellular responses to DNA damage. *Cancer Res.*, **55**, 5991–6001.
37. Boder, E. and Sedgwick, R.P. (1958) Ataxia-telangiectasia; a familial syndrome of progressive cerebellar ataxia, oculocutaneous telangiectasia and frequent pulmonary infection. *Pediatrics*, **21**, 526–554.
38. Yang, Y. and Herrup, K. (2005) Loss of neuronal cell cycle control in ataxia-telangiectasia: a unified disease mechanism. *J. Neurosci.*, **25**, 2522–2529.
39. Lavezzi, A.M., Ottaviani, G., Terni, L. and Matturri, L. (2006) Histological and biological developmental characterization of the human cerebellar cortex. *Int. J. Dev. Neurosci.*, **24**, 365–371.
40. McKinnon, P.J. (2012) ATM and the molecular pathogenesis of ataxia telangiectasia. *Annu. Rev. Pathol.*, **7**, 303–321.
41. Bottini, A.R., Gatti, R.A., Wirenfeldt, M. and Vinters, H.V. (2012) Heterotopic Purkinje cells in ataxia-telangiectasia. *Neuropathology*, **32**, 23–29.
42. Schubert, R., Reichenbach, J. and Zielen, S. (2005) Growth factor deficiency in patients with ataxia telangiectasia. *Clin. Exp. Immunol.*, **140**, 517–519.
43. Egerton, T., Thingstad, P. and Helbostad, J.L. (2014) Comparison of programs for determining temporal-spatial gait variables from instrumented walkway data: PKmas versus GAITRite. *BMC Res. Notes*, **7**, 542.
44. Schniepp, R., Wuehr, M., Neuhaeusser, M., Kamenova, M., Dimitriadis, K., Klopstock, T., Strupp, M., Brandt, T. and Jahn, K. (2012) Locomotion speed determines gait variability in cerebellar ataxia and vestibular failure. *Mov. Disord.*, **27**, 125–131.
45. Sorsdahl, A.B., Moe-Nilssen, R. and Strand, L.I. (2008) Test-retest reliability of spatial and temporal gait parameters in

children with cerebral palsy as measured by an electronic walkway. *Gait Posture*, **27**, 43–50.
46. Rinehart, N.J., Tonge, B.J., Iansek, R., McGinley, J., Brereton, A.V., Enticott, P.G. and Bradshaw, J.L. (2006) Gait function in newly diagnosed children with autism: Cerebellar and basal ganglia related motor disorder. *Dev. Med. Child Neurol.*, **48**, 819–824.
47. Serrao, M., Pierelli, F., Ranavolo, A., Draicchio, F., Conte, C., Don, R., Di Fabio, R., LeRose, M., Padua, L., Sandrini, G. *et al.* (2012) Gait pattern in inherited cerebellar ataxias. *Cerebellum*, **11**, 194–211.
48. Stephenson, J., Zesiewicz, T., Gooch, C., Wecker, L., Sullivan, K., Jahan, I. and Kim, S.H. (2015) Gait and balance in adults with Friedreich's ataxia. *Gait Posture*, **41**, 603–607.
49. Sedgewick, R.P. and Boder, E. (1991), *Handbook of Clinical Neurology*, In Vinken, P., Bruyn, G. and Klawans, H., (eds), Elsevier, New York, USA, Vol. 60, pp. 347–423.
50. Chiesa, N., Barlow, C., Wynshaw-Boris, A., Strata, P. and Tempia, F. (2000) Atm-deficient mice Purkinje cells show age-dependent defects in calcium spike bursts and calcium currents. *Neuroscience*, **96**, 575–583.
51. Barlow, C., Ribaut-Barassin, C., Zwingman, T.A., Pope, A.J., Brown, K.D., Owens, J.W., Larson, D., Harrington, E.A., Haeberle, A.M., Mariani, J. *et al.* (2000) ATM is a cytoplasmic protein in mouse brain required to prevent lysosomal accumulation. *Proc. Natl. Acad. Sci. U.S.A.*, **97**, 871–876.
52. Meneret, A., Ahmar-Beaugendre, Y., Rieunier, G., Mahlaoui, N., Gaymard, B., Apartis, E., Tranchant, C., Rivaud-Pechoux, S., Degos, B., Benyahia, B. *et al.* (2014) The pleiotropic movement disorders phenotype of adult ataxia-telangiectasia. *Neurology*, **83**, 1087–1095.
53. Wells, C.E. and Shy, G.M. (1957) Progressive familial choreoathetosis with cutaneous telangiectasia. *J. Neurol. Neurosurg. Psychiatry*, **20**, 98–104.
54. Oka, A. and Takashima, S. (1998) Expression of the ataxia-telangiectasia gene (ATM) product in human cerebellar neurons during development. *Neurosci. Lett.*, **252**, 195–198.
55. Lee, Y., Katyal, S., Downing, S.M., Zhao, J., Russell, H.R. and McKinnon, P.J. (2012) Neurogenesis requires TopBP1 to prevent catastrophic replicative DNA damage in early progenitors. *Nat. Neurosci.*, **15**, 819–826.
56. Sahama, I., Sinclair, K., Pannek, K., Lavin, M. and Rose, S. (2014) Radiological imaging in ataxia telangiectasia: a review. *Cerebellum*, **13**, 521–530.
57. Tavani, F., Zimmerman, R.A., Berry, G.T., Sullivan, K., Gatti, R. and Bingham, P. (2003) Ataxia-telangiectasia: the pattern of cerebellar atrophy on MRI. *Neuroradiology*, **45**, 315–319.
58. Hayashi, M., Miyata, R. and Tanuma, N. (2012) Oxidative stress in developmental brain disorders. *Adv. Exp. Med. Biol.*, **724**, 278–290.
59. Pfeiffer, H. (2008) Forensic neuropathology: a practical review of the fundamentals. In Itabashi, H.H., Andrews, J.M., Tomiyasu, U., Erlich, S.S., and Sathyavagiswaran, L. (eds), Academic Press, Burlington, MA, USA, 2007, *Int. J. Legal Med.*, **122**, 269–269.
60. Kamiya, M., Yamanouchi, H., Yoshida, T., Arai, H., Yokoo, H., Sasaki, A., Hirato, J., Nakazato, Y., Sakazume, Y. and Okamoto, K. (2001) Ataxia telangiectasia with vascular abnormalities in the brain parenchyma: report of an autopsy case and literature review. *Pathol. Int.*, **51**, 271–276.
61. Nakayama, T., Sato, Y., Uematsu, M., Takagi, M., Hasegawa, S., Kumada, S., Kikuchi, A., Hino-Fukuyo, N., Sasahara, Y., Haginoya, K. *et al.* (2014) Myoclonic axial jerks for diagnosing atypical evolution of ataxia telangiectasia. *Brain Dev.*, in press.
62. Onodera, O. (2006) Spinocerebellar ataxia with ocular motor apraxia and DNA repair. *Neuropathology*, **26**, 361–367.
63. Leuzzi, V., Elli, R., Antonelli, A., Chessa, L., Cardona, F., Marcucci, L. and Petrinelli, P. (1993) Neurological and cytogenetic study in early-onset ataxia-telangiectasia patients. *Eur. J. Pediatr.*, **152**, 609–612.
64. Saunders-Pullman, R., Raymond, D., Stoessl, A.J., Hobson, D., Nakamura, K., Pullman, S., Lefton, D., Okun, M.S., Uitti, R., Sachdev, R. *et al.* (2012) Variant ataxia-telangiectasia presenting as primary-appearing dystonia in Canadian Mennonites. *Neurology*, **78**, 649–657.
65. Walker, S.C., Shin, T., Zaunbrecher, G.M., Romano, J.E., Johnson, G.A., Bazer, F.W. and Piedrahita, J.A. (2002) A highly efficient method for porcine cloning by nuclear transfer using in vitro-matured oocytes. *Cloning Stem Cells*, **4**, 105–112.
66. Kim, Y.J., Ahn, K.S., Kim, M., Kim, M.J., Park, S.M., Ryu, J., Ahn, J.S., Heo, S.Y., Kang, J.H., Choi, Y.J. *et al.* (2014) Targeted disruption of Ataxia-telangiectasia mutated gene in miniature pigs by somatic cell nuclear transfer. *Biochem. Biophys. Res. Commun.*, **452**, 901–905.
67. Beraldi, R., Li, X., Martinez Fernandez, A., Reyes, S., Secreto, F., Terzic, A., Olson, T.M. and Nelson, T.J. (2014) Rbm20-deficient cardiogenesis reveals early disruption of RNA processing and sarcomere remodeling establishing a developmental etiology for dilated cardiomyopathy. *Hum. Mol. Genet.*, **23**, 3779–3791.
68. Getty, A., Kovacs, A.D., Lengyel-Nelson, T., Cardillo, A., Hof, C., Chan, C.H. and Pearce, D.A. (2013) Osmotic stress changes the expression and subcellular localization of the Batten disease protein CLN3. *PLoS ONE*, **8**, e66203.
69. Evans, H.J. and O'Riordan, M.L. (1975) Human peripheral blood lymphocytes for the analysis of chromosome aberrations in mutagen tests. *Mutat. Res.*, **31**, 135–148.
70. Llerena, J. Jr, Murer-Orlando, M., McGuire, M., Zahed, L., Sheridan, R.J., Berry, A.C. and Bobrow, M. (1989) Spontaneous and induced chromosome breakage in chorionic villus samples: a cytogenetic approach to first trimester prenatal diagnosis of ataxia telangiectasia syndrome. *J. Med. Genet.*, **26**, 174–178.
71. Ho, M., Post, C.M., Donahue, L.R., Lidov, H.G., Bronson, R.T., Goolsby, H., Watkins, S.C., Cox, G.A. and Brown, R.H. Jr (2004) Disruption of muscle membrane and phenotype divergence in two novel mouse models of dysferlin deficiency. *Hum. Mol. Genet.*, **13**, 1999–2010.
72. Ando, Y., Ichihara, N., Takeshita, S., Saito, Y., Kikuchi, T. and Wakasugi, N. (2004) Histological and ultrastructural features in the early stage of Purkinje cell degeneration in the cerebellar calcification (CC) rat. *Exp. Anim.*, **53**, 81–88.
73. Gundersen, H.J. (1988) The nucleator. *J. Microsc.*, **151**, 3–21.
74. Gundersen, H.J., Jensen, E.B., Kieu, K. and Nielsen, J. (1999) The efficiency of systematic sampling in stereology—reconsidered. *J. Microsc.*, **193**, 199–211.
75. Gibson-Corley, K.N., Olivier, A.K. and Meyerholz, D.K. (2013) Principles for valid histopathologic scoring in research. *Vet. Pathol.*, **50**, 1007–1015.
76. Meyerholz, D.K., Stoltz, D.A., Namati, E., Ramachandran, S., Pezzulo, A.A., Smith, A.R., Rector, M.V., Suter, M.J., Kao, S., McLennan, G. *et al.* (2010) Loss of cystic fibrosis transmembrane conductance regulator function produces abnormalities in tracheal development in neonatal pigs and young children. *Am. J. Respir. Crit. Care Med.*, **182**, 1251–1261.
77. Mittal, K.R. and Olszewski, W.A. (1985) Widening of inter-Purkinje cell distances in association with corpora amylacea. *J. Gerontol.*, **40**, 700–702.
78. Huxham, F., Gong, J., Baker, R., Morris, M. and Iansek, R. (2006) Defining spatial parameters for non-linear walking. *Gait Posture*, **23**, 159–163.